Scattering of Ions
V. Elastic Scattering of the Symmetric Rare Gas Ion — Rare Gas Atom Systems

H.-U. Mittmann and H.-P. Weise

Hahn-Meitner-Institut für Kernforschung Berlin GmbH, Bereich Strahlenchemie, Berlin

(Z. Naturforsch. **29 a**, 400–410 [1974]; received 14 December 1973)

Differential cross-sections for the elastic scattering of Ne^+ on Ne, Ar^+ on Ar, Kr^+ on Kr, and Xe^+ on Xe have been measured. In the lab.-energy range from 3 eV up to 30 eV a rainbow maximum was observed and attributed to the attractive ground state potentials of these systems. From the angular positions of the primary rainbows the potential depths were derived. In the case of Ne_2^+ and Ar_2^+ these values are compared with the results of quantum chemical calculations and of semi-empirical estimates. From lowest energies up to $E_L = 200$ eV g-u-interference oscillations were observed for all systems. In the case of $Ne^+ - Ne$ two oscillatory structures with different frequencies were detected and attributed to interference between Π-states and Σ-states, respectively. With increasing atomic number of the rare gas atoms the g-u-structure becomes increasingly irregular. The measured angular distances were used to derive the potential energy difference between the interfering molecular states. The evaluation was carried out by varying parameters of analytical model potentials for the lower lying state and the difference potential until the quantum mechanically calculated differential cross-section agreed with the experimental one within the experimental error. In the case of Ne_2^+ and Ar_2^+ the results are compared with ab initio calculations and experimental results of other authors. For $Kr^+ - Kr$ and $Xe^+ - Xe$ a fit at all energies could not be obtained with a single set of parameters. This effect and the high irregularity of the experimental curves are attributed to fine structure splitting of the molecular states via the strong spin-orbit coupling in Kr and Xe.

I. Introduction

In a previous communication the elastic scattering of He^+ on He at low energies was reported [1]. A well resolved rainbow structure with superimposed rapid oscillations could be observed and at all angles g-u-interference undulations were detected. From the measured data the potential curve of the $^2\Sigma_u^+$ state could be determined. The potential depth ε was obtained as 2.55 eV the equilibrium distance r_m as 1.05 Å.

In the present investigation measurements are reported on the system $Ne^+ - Ne$, $Ar^+ - Ar$, $Kr^+ - Kr$, and $Xe^+ - Xe$. All systems exhibited a primary rainbow and g-u-interference. The apparatus has been described elsewhere [2]. The energy width of the primary ion beam was about 0.5 eV, the angular resolution was varied between 0.7° and 1.4°.

II. The Rainbow Structure

The primary rainbow could be detected for all systems in the energy range from 3 eV to 30 eV. Figure 1 shows two typical differential cross-sections for the system $Ne^+ - Ne$. The primary rainbow is indicated by an arrow. The extrema left and right of the arrow are attributed to g-u-interference. A

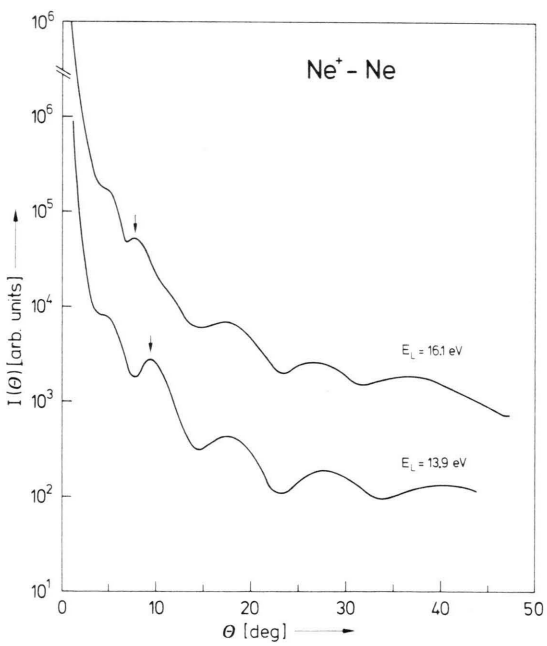

Fig. 1. Differential cross-sections for elastic scattering of Ne^+ on Ne at $E_L = 13.9$ eV and $E_L = 16.1$ eV (lab.-system). The arrows indicate the position of the primary rainbow maximum.

Reprint requests to Dr. H.-P. Weise, HMI-Strahlenchemie, *1000 Berlin 39*, Glienicker Str. 100.

distinction between the two different types of oscillations can be made by measuring the energy dependence of the angular positions of the extrema. The position of the angle of the primary rainbow ϑ_R varies with energy E_c approximately according to the formula

$$\vartheta_R E_c/\varepsilon \approx \text{const}.$$

The energy dependence of the g-u-oscillations is much weaker. By varying the energy the primary rainbow shifts relative to the g-u-structure which can be considered to be approximately stationary. In the lower curve of Fig. 1 the energy is chosen such that the rainbow coincides with a maximum of the g-u-oscillations thus resulting in a strongly pronounced maximum. In the upper curve the primary rainbow coincides with a minimum of the g-u-structure giving nearly complete cancellation. Because of the strong disturbance of the primary rainbow by the g-u-oscillations no further attempt was made to resolve secondary rainbows. Similar conditions apply for the other systems.

In order to determine the potential depth of the attractive part of the potential the angular positions of the primary rainbows were measured at a number of energies and plotted as a function of energy. Because of the g-u-oscillations the error in the determination of the position of the primary rainbow angle may be considerable. Thus the evaluation was made using an averaging function $\vartheta_R = \vartheta_R(E_c)$. Since only the primary rainbow has been measured the potential depth ε, the equilibrium distance r_m and the potential shape could not be determined independently. Thus, additional information was required. For the systems $Ne^+ - Ne$ and $Ar^+ - Ar$ the equilibrium distance and the shape of the reduced potential could be taken from a calculation by Gilbert and Wahl [3]. The reduced potential was obtained by fitting a modified Morse potential according to Eq. (10) to the theoretical potential curve. To evaluate the measurements for the systems $Kr^+ - Kr$ and $Xe^+ - Xe$ the reduced Morse potential of the system $Ar^+ - Ar$ was used. The equilibrium distance for the system $Xe^+ - Xe$ was taken from an estimate from Mulliken [4]. For the system $Kr^+ - Kr$ the mean value of the equilibrium distances of $Ar^+ - Ar$ and $Xe^+ - Xe$ was used. Thus, in the analytical expression for the potential only one free parameter, the potential depth, is left. With this potential differential cross-sections were calculated quantum mechanically.

ε was varied until agreement between the measured and calculated positions of the primary rainbow maxima was achieved. The results are given in Table I.

Table I. Potential parameters of the $^2\Sigma_u^+$-state for the symmetric rare gas ion — rare gas atom systems.

	ε/eV	r_m/Å	G_1	G_2	ε/eV	r_m/Å
He^+-He	2.55 [d]	1.05 [d]	2.35 [d]	0.90 [d]	2.32 [a]	1.09 [a]
Ne^+-Ne	1.30	1.69 [b]	3.6	1.0	1.65 [b]/1.1 [c]	1.69 [b]
Ar^+-Ar	1.34	2.43 [b]	4.0	0.95	1.25 [b]/1.4 [c]	2.43 [b]
Kr^+-Kr	1.21	2.6	4.0	0.95	1.20 [c]	—
Xe^+-Xe	0.99	2.85 [c]	4.0	0.95	1.0 [c]	2.85 [c]

[a] Gupta-Matsen [18].
[b] Gilbert-Wahl [3].
[c] Mulliken [4].
[d] Weise et al. [1].

In the first column the experimental potential depths are given, in the second column the r_m-values used. The two columns following contain the form parameters which determine the modified Morse potential. The remaining columns contain the results of other authors. The overall error in the potential depth is estimated to be approximately ± 0.1 eV.

For the system $Ne^+ - Ne$ the potential depth calculated by Gilbert and Wahl is about 30% larger than the experimental value. Using the calculated reduced potential curve no agreement between the theoretical and the experimental potential depths can be obtained. This discrepancy may result from use of an incorrect shape for the reduced potential or an incorrect equilibrium distance in evaluating the experimental results. However changes in the potential shape and in r_m have only limited influence on the ε-value obtained. We suggest therefore that the potential depth of the calculation is too large. This suspicion is supported by the estimate of Mulliken (Table I). In comparison with the value for $Ar^+ - Ar$, the equilibrium distance of the calculation seems to be too small.

For the system $Ar^+ - Ar$ the agreement between the experimental and the theoretical values is satisfying. The deviations are within the experimental error. For the systems $Kr^+ - Kr$ and $Xe^+ - Xe$ no calculations appear to have been made. The values obtained in this investigation agree very well with the estimates of Mulliken.

III. The g-u-Oscillations

a) $He^+ - He$

G-u-interference was first detected for the elastic scattering of He^+ on He. These oscillations in the

differential cross-section are a consequence of the symmetry of the nuclear charges of the two interacting particles. Thus two different molecular states, $^2\Sigma_u^+$ and $^2\Sigma_g^+$ originate from the state $He^+(^2S_{1/2}) + He(^1S_0)$ of the separated atoms on mutual approach. The electronic wave functions of the attractive $^2\Sigma_u^+$-state and the repulsive $^2\Sigma_g^+$-state are antisymmetric and symmetric respectively under inversion at the center of symmetry of the He_2^+-molecule.

The occurence of g-u-interference can be understood qualitatively by using a semi-classical model[7]. When the two particles approach each other the degeneracy of the electronic wave function is removed and the wave packet which describes the scattering process splits into two coherent parts which are scattered differently due to the different potential curves of the states $^2\Sigma_u^+$ and $^2\Sigma_g^+$. Since the classical deflection functions for the two potential curves are different, two different impact parameters b_g and b_u belong to each scattering angle ϑ. The corresponding coherently scattered partial waves interfere with each other, thus giving rise to well pronounced oscillations in the differential elastic cross-section. The described interference phenomenon is similar to the interference of two coherent electromagnetic waves behind a double slit system. The distance between the slits corresponds to the difference $|b_g - b_u|$ of the impact parameters which belong to the same scattering angle.

The semi-classical treatment of the g-u-oscillations by analogy with the wave optical formula gives the following relation for the angular separation of two extrema:

$$\Delta\vartheta = 2\pi/k\,|b_g - b_u| \qquad (1)$$

(k = wave number). (This formula is valid only if the two deflection functions have the same sign in that b-region which corresponds to the scattering angle considered. In this region, the potentials are either both attractive or repulsive). $|b_g - b_u|$ depends on the difference in the deflection functions and thus on the difference of the two potentials $\Delta V = V_g - V_u$.

The larger ΔV, the larger is the difference $|b_g - b_u|$ for a fixed scattering angle ϑ. Consequently, according to Eq. (1) the angular separation of the oscillations in the vicinity of ϑ decreases with increasing difference potential. Thus from the experimentally determined angular separations information about the difference potential can be obtained.

The wave mechanical treatment of the $He^+ - He$ scattering gives the following formula for the differential cross-section[7]:

$$I(\vartheta) = \tfrac{1}{4}\,|f_g(\vartheta) + f_u(\vartheta)|^2, \qquad (2)$$

f_g: scattering amplitude for the $^2\Sigma_g^+$ potential,
f_u: scattering amplitude for the $^2\Sigma_u^+$ potential.

The interference term of the two scattering amplitudes describes the g-u-oscillations. For the scattering of $^4He^+$ on ^4He the two helium nuclei constitute a system of identical bosons. Thus the wave function which describes the scattering process must be symmetric under interchange of the two nuclei. The symmetrization leads to the more complicated expression:

$$I(\vartheta) = \tfrac{1}{4}\,|f_g(\vartheta) + f_u(\vartheta) + f_g(\pi - \vartheta) - f_u(\pi - \vartheta)|^2. \qquad (3)$$

The additional term $f_g(\pi - \vartheta) - f_u(\pi - \vartheta)$ gives rise to an additional interference structure in the differential cross-section. Oscillations due to the symmetry of the nuclei have been observed for the scattering of $^4He^+$ on ^4He experimentally[6]. For the system $^4He^+ - {}^3He$ with unequal nuclei no such oscillations have been found in accordance with the theory. In this case the simple relation Eq. (2) is valid.

b) $Ne^+ - Ne$, $Ar^+ - Ar$, $Kr^+ - Kr$, $Xe^+ - Xe$

In contrast to the He^+ ion the ground state of the heavier rare gas ions is a ^2P state. According to the Wigner-Witmer combination rules, from the asymptotic state

$$X^+(^2P^0) + X(^1S^e)$$

of the separated particles four potential curves arise when the particles approach each other[8]. They have the following symmetries: $^2\Sigma_u^+$, $^2\Pi_g$, $^2\Pi_u$, $^2\Sigma_g^+$. The projection of the electronic orbital angular momentum on the axis of symmetry is zero for the Σ states and ± 1 for the Π-states. Thus, the Π-states are doubly degenerate, the Σ-states are not degenerate. The energetic sequence of the four states can be deduced from their MO-configurations.

$(\sigma g)\ (\Pi_u)^4\,(\Pi_g)^4\,(\sigma_u)^2\quad {}^2\Sigma_g^+$
$(\sigma g)^2\,(\Pi_u)^3\,(\Pi_g)^4\,(\sigma_u)^2\quad {}^2\Pi_u$
$(\sigma g)^2\,(\Pi_u)^4\,(\Pi_g)^3\,(\sigma_u)^2\quad {}^2\Pi_g$
$(\sigma g)^2\,(\Pi_u)^4\,(\Pi_g)^4\,(\sigma_u)\quad {}^2\Sigma_u^+$

↑ E

In Fig. 2 the potential curve diagram for the system Ne_2^+ is shown. The ground state $^2\Sigma_u^+$ has a well

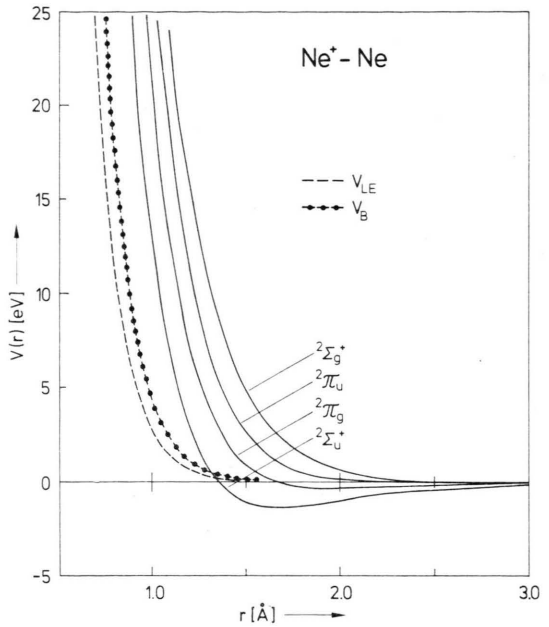

Fig. 2. Potential energy diagram of the four lowest states of Ne_2^+. Solid line curves: Experimental results of this work. Dashed line: Results from Lane and Everhart, extrapolated to large distances [13]. Dotted curve: Ne_2^+-potential calculated using a formula from Bohr [13].

pronounced potential minimum, but the other potential curves are repulsive at intermediate distances. The wave packet which describes the scattering process splits into four parts which are scattered according to the four different potential curves. The partial waves belonging to the $^2\Sigma_g^+$- and the $^2\Sigma_u^+$-states interfere with each other just as the partial waves belonging to the $^2\Pi_g$- and $^2\Pi_u$-states. There is no interference between the Σ- and the Π-partial waves because of the difference between the components of the orbital angular momentum along the axis of symmetry. Thus there are $\Sigma_g - \Sigma_u$ and $\Pi_g - \Pi_u$-interferences in the differential cross-section, but no $\Sigma - \Pi$-oscillations.

The potential difference of the Σ-states

$$\Delta V_\Sigma = V^{2}{}_{\Sigma_g^+} - V^{2}{}_{\Sigma_u^+}$$

is much larger than the difference of the Π-states

$$\Delta V_\Pi = V_{^2\Pi_u} = V_{^2\Pi_g}.$$

Thus the $\Sigma_g - \Sigma_u$-oscillations have a much smaller period than the $\Pi_g - \Pi_u$-oscillations. The relative amplitudes of the two interference structures are determined by the ratio of the probabilities that the system forms a Σ-state or a Π-state. The Σ-states are not degenerate, the Π-states are doubly degenerate ($\Lambda = \pm 1$). Consequently, the ratio of the probabilities is 1:2 and the differential cross-section is described by Equation (4).

$$I(\vartheta) = \tfrac{1}{3} I_\Sigma(\vartheta) + \tfrac{2}{3} I_\Pi(\vartheta) \tag{4}$$

with

$$I_\Sigma(\vartheta) = \tfrac{1}{4} \left| f_{\Sigma_g}(\vartheta) + f_{\Sigma_u}(\vartheta) \right|^2$$
$$I_\Pi(\vartheta) = \tfrac{1}{4} \left| f_{\Pi_g}(\vartheta) + f_{\Pi_u}(\vartheta) \right|^2 .$$

In contrast to Eq. (3) the above relationship does not take nuclear symmetry into account. This approximation is sufficient for the evaluation of the experiments for the following reasons:

1) Oscillations due to nuclear symmetry effects could not be observed for the heavier rare gas ion-rare gas atom systems since the angular separation of the oscillations is very small.
2) The angular positions of the g-u-undulations are not disturbed by nuclear symmetry oscillations since the latter have a much smaller period. Consequently the simpler expressions of Eq. (4) give the same angular positions of the g-u-undulations as the more complicated formula which allows for the nuclear symmetry.
3) The gases used in the experiments contained their isotopes in natural abundance.

For the heavy rare gases Kr and Xe the spin-orbit coupling becomes important. The stronger coupling leads to a fine structure splitting of the Π-states. In this case the component of orbital angular momentum along the symmetry axis is no longer a good quantum number and the total angular momentum must be used instead [8]. Consequently the designations $^2\Sigma$ and $^2\Pi$ lose their sense and must be replaced by new symbols. The sequence of terms is the following:

$$(^2\Sigma_u^+)\,\tfrac{1}{2}\,u\,,\quad (^2\Pi_g)\,\tfrac{3}{2}g\,,\quad (^2\Pi_g)\,\tfrac{1}{2}\,g\,,\quad (^2\Pi_u)\,\tfrac{3}{2}u\,,$$
$$(^2\Pi_u)\,\tfrac{1}{2}\,u\,,\quad (^2\Sigma_g^+)\,\tfrac{1}{2}\,g\,.$$

The symbols in brackets give the correlations with the states for the case of vanishing spin – orbit coupling. The energetic sequence of the 3/2- and 1/2-states can be deduced from Hund's rules. In Fig. 3 the six resulting potential curves are plotted together with their asymptotic behaviour. g-u-oscillations arise only from coherent scattering by g-u-states with the same total electronic angular mo-

mentum. The wave packets originating from the $X^+(^2P^0_{3/2}) + X(^1S_0{}^e)$ asymptotic state and the $X^+(^2P^0_{1/2}) + X(^1S_0{}^e)$ state are not coherent. Thus from Fig. 3 three groups of oscillations with different frequencies might be expected.

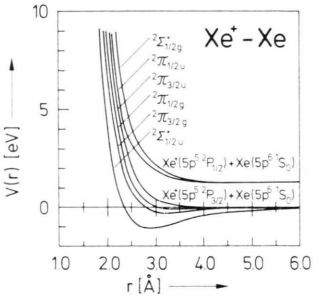

Fig. 3. Potential curve diagram of the six lowest states of Xe_2^+.

IV. The Method of Evaluation

a) Fundamental Equations

To evaluate the experiments, Eq. (4) and model potentials with adjustable parameters were used. For each set of parameters, the differential cross-section was calculated and the angular positions of the interference extrema were compared with the experimental data. The potential parameters were varied until agreement between the calculated and the experimental angular positions was obtained within the uncertainty of the measurement. The scattering amplitudes were calculated by partial wave analysis using WKB-phases [9, 10].

$$f(\vartheta) = \frac{1}{2ik}\sum_{l=0}^{\infty}(2l+1)\,(e^{2i\eta_l}-1)\,P_l(\cos\vartheta),$$

η_l: scattering phases, P_l: Legendre polynomials,

$$\eta_l^{\mathrm{WKB}} = \frac{\pi}{2}(l+\tfrac{1}{2}) - k\,r_c + k\int_{r_c}^{\infty}\left(\sqrt{1-\frac{V(r)}{E_c}-\frac{b_l^2}{r^2}}-1\right)\mathrm{d}r, \qquad (5)$$

μ = reduced mass,
E_c = energy in the center of mass system,
r_c = classical turning point.

For the numerical calculation of the WKB phases, Eq. (5) was rearranged in the following way:

$$\eta_l^{\mathrm{WKB}} = k\left[-r_c - \int_{r_c}^{r_1}\frac{\left(\frac{V(r)}{E_c}+\frac{b_l^2}{r^2}\right)\mathrm{d}r}{1+\sqrt{1-\frac{V(r)}{E_c}-\frac{b_l^2}{r^2}}} + \frac{b_l^2}{r_1+\sqrt{r_1^2-b_l^2}} + b_l\,\mathrm{arc\,tg}\,\frac{1}{b_l}\sqrt{r_1^2-b_l^2}\right]. \qquad (6)$$

This relation is obtained by splitting the range of integration into two parts from r_c up to r_1 and from r_1 up to infinity. r_1 was chosen such that $V(r_1)/E_c < 10^{-6}$. For $r > r_1$ the term $V(r)/E_c$ is of the same order of magnitude as the computational inaccuracy. Neglecting $V(r)/E_c \mid r > r_1$, the integral can be solved explicitely in the range from r_1 to infinity. For the numerical computation of the integral from r_c to r_1 the Newton-Cotes-formula was used.

For very large angular momenta l the Jeffreys-Born-phases are a sufficiently good approximation for the WKB phases [11].

$$\eta_l^{\mathrm{JB}} = -\frac{k}{2}\int_{b_l}^{\infty}\frac{[V(r)/E_c]\,\mathrm{d}r}{\sqrt{1-b_l^2/r^2}}. \qquad (7)$$

The model potentials used are sums of exponential functions. In this case, the JB-phases can be calculated explicitely. For the potential

$$V(r) = C\,e^{-\alpha r}$$

the JB-phases are found to be:

$$\eta_b = -k\,b\,C\,K_1(b\,\alpha)/2\,E_c \qquad (8)$$

K_1: modified Bessel-function.

For the computation of $K_1(b\cdot\alpha)$ an asymptotic expansion with only a few terms has been used [12]. Because of the linear dependence of the JB-phases on the potential, the total phase is the sum of the contributions of the different exponential functions.

For evaluation of the experiments the following analytical potentials were used:

$$V_{\Sigma_g}(r) = V_{\Sigma_u}(r) + a_\Sigma\,e^{-\alpha_\Sigma r} = V_{\Sigma_u}(r) + \Delta V_\Sigma(r),$$
$$V_{\Pi_u}(r) = V_{\Pi_g}(r) + a_\Pi\,e^{-\alpha_\Pi r} = V_{\Pi_g}(r) + \Delta V_\Pi(r). \qquad (9)$$

The difference potentials $\Delta V_\Sigma(r)$ and $\Delta V_\Pi(r)$ were approximated by simple exponential functions. For the description of the ground state potentials $V\,^2\Sigma_u^+(r)$ a modified Morse potential has been used:

$$V(\varrho) = \varepsilon[e^{2G_1G_2(1-\varrho)} - 2\,e^{G_1G_2(1-\varrho)}]$$
$$G_2 = 1 \quad \text{for} \quad \varrho < 1,$$
$$G_2 \neq 1 \quad \text{for} \quad \varrho \geqq 1, \qquad (10)$$

ε: potential depth; r_m: equilibrium distance.

The $V\,^2\Sigma_u^+$ potentials of the different systems were determined from the measurement of the rainbow structures. For the Π_g-states a simple Morse potential was used where a flat potential well accounts for the polarization of the target atom by the radial electric field of the ion.

b) Influence of the Potential Parameters on the Position of the Extrema of the g-u-Oscillations

For the evaluation of the experiments the measured angular positions of the g-u-extrema were converted to the center of mass system and plotted as a function of the number N (maxima: N = integer, minima: N = half-integer). N was normalized so that $N=0$ for the maximum at $\vartheta=0$ which is due to constructive interference of partial waves with very large angular momenta. Since this maximum is disturbed by the primary ion beam profile the experimental curves $\vartheta(N)$ had to be extrapolated to zero scattering angle. For the $\Pi_{g\text{-}u}$-oscillations in most cases the extrema could be detected starting from the maximum $N=1$. The $\Sigma_{g\text{-}u}$-oscillations of the system $Ne^+ - Ne$ could not be detected for $N<3$.

Using the semi-classical relation (1), the influence of the potential parameters on the calculated angular positions of the g-u-oscillations can be discussed. If the parameter a [see Eq. (9)] is made smaller (leaving all other parameters constant), the difference between the two potential curves is diminished. Consequently the difference between the corresponding classical deflection functions also decreases. For each scattering angle ϑ the difference between the corresponding impact parameters $|b_g - b_u|$ decreases and according to Eq. (1) the angular separation of the oscillations increases. The influence of the other parameters can be discussed in a similar way. The results are summarized in Table II.

Table II. Influence of the potential parameters [Eq. (9) and Eq. (10)] on the angular separation of the g-u-oscillations. These relations are demonstrated by the calculated curves shown in Figure 4.

parameter	a	α	ε	r_m	G_1
direction of change of the parameter	<	<	<	<	<
direction of change of the angular separation	>	<	<	<	<

The shape of the ground potential curve is reflected in the shape of the function $\vartheta(N)$, if the difference potential remains constant. The greater the curvature of the ground potential the greater the curvature of the $\vartheta(N)$ plot (Figure 4).

The five potential parameters given in the table have approximately the same or the reverse influence on the shape of the curve $\vartheta(N)$. Thus they cannot be determined independently from the experimental data with sufficient accuracy. To determine the difference potential, a suitable assumption about the ground potential had to be made.

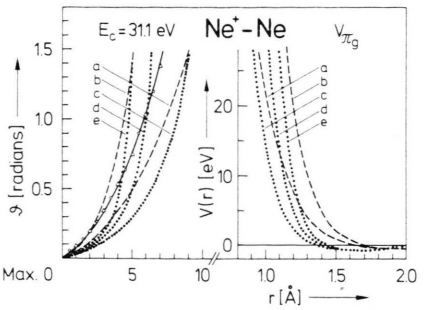

Fig. 4. Influence of different parameters (see Eq. (9) and (10)) on the shape of the $^2\Pi_g$-potential curve and on the corresponding functions $\vartheta(N)$, describing the positions of the extrema of the g-u-oscillations at $E_c=31.1$ eV. $\varepsilon=0.3$ eV, $a=152.8$, $\alpha=2.81$, $G_2\equiv 1$ for all curves. a: $G_1=4.5$, $r_m=2.0$ Å; b: $G_1=5.5$, $r_m=2.0$ Å; c: $G_1=5.5$, $r_m=1.6$ Å; d: $G_1=6.5$, $r_m=1.6$ Å; e: $G_1=7.5$, $r_m=1.6$ Å. The solid line curve represents the best fit to the experimental data. The corresponding potentials are given by Equations (9) and (10). ○ and △ represent experimental data (○: minimum, △: maximum).

V. Experimental Results and Discussion

a) $Ne^+ - Ne$

Differential cross-sections for the system $Ne^+ - Ne$ have been measured in the energy range from $E_L = 2.4$ eV to 170 eV. In the whole range of angles and energies $\Pi_{g\text{-}u}$-interferences could be observed. The $\Sigma_{g\text{-}u}$-oscillations could be detected in the energy range from $E_L = 60$ eV to 100 eV. Figure 5 shows a typical curve for the energy $E_L = 62.2$ eV. The $\Pi_{g\text{-}u}$-interference extrema are well resolved. Comparing their amplitudes with each other, no marked

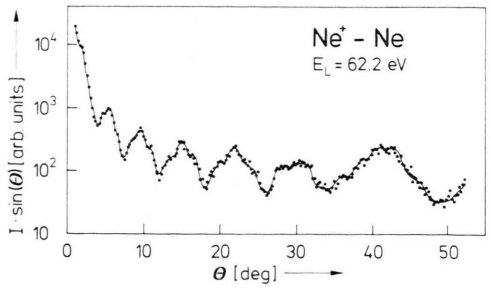

Fig. 5. Differential elastic scattering cross-section for $Ne^+ - Ne$ at $E_L=62.2$ eV exhibiting the low frequency $\Pi_g - \Pi_u$-oscillations and the high frequency $\Sigma_g - \Sigma_u$-oscillations.

quenching is observed as a function of the scattering angle. In the whole range of angles the $\Pi_{g\text{-}u}$-interference undulations are superimposed by $\Sigma_{g\text{-}u}$-oscillations. Since the potential difference between the Σ-states is larger than between the Π-states, the frequency of the $\Sigma_{g\text{-}u}$-oscillations is much smaller than the frequency of the $\Pi_{g\text{-}u}$-oscillations. The relation of the amplitudes of the $\Pi_{g\text{-}u}$- and $\Sigma_{g\text{-}u}$-oscillations is greater than the theoretical value 2:1. This is certainly due to the finite angular resolution of the apparatus. On account of the small angular distance of the $\Sigma_{g\text{-}u}$-oscillations their amplitudes are much more damped than those of the $\Pi_{g\text{-}u}$-oscillations.

In order to determine the difference potential from the $\Sigma_{g\text{-}u}$-oscillations the $^2\Sigma_u^+$-potential curve of the ground state with the parameters according to Table I has been used. Since the $\Sigma_{g\text{-}u}$-oscillations are determined essentially by the repulsive part of the ground potential, a reasonable assumption about the shape of the ground potential for small distances had to be made. It was assumed that the potential function used to describe the observed rainbow scattering (which is determined by the attractive part) is also valid for small distances. By variation of the parameters a and α of the difference potential in the whole angular range good agreement between the calculated curves $\vartheta(N)$ and the experimental curves could be obtained. With the same set of parameters the experimental results for all collision energies used could be described. The results are:

$$V_{2\Sigma_g^+} = V_{2\Sigma_u^+} + 256.0\, e^{-2.51r} \quad \text{with} \quad (11)$$

$$V_{2\Sigma_u^+} = 1.3\,(e^{7.2(1-\varrho)} - 2\, e^{3.6(1-\varrho)}) \quad \text{with} \quad \varrho = r/1.69\,.$$

For the evaluation of the $\Pi_{g\text{-}u}$-oscillations an assumption about the ground potential had to be made also. For the $^2\Pi_g$-potential no experimental information could be obtained. Hence the potential was chosen arbitrarily to fulfill the condition that the $^2\Pi_g$-potential curve and the resulting $^2\Pi_u$-curve lie between the two Σ-potentials, according to the required energy sequence of the states (chapter III). For a first trial the potential $V_{2\Pi_g}$ was assumed to be a screened Coulomb potential. The calculations with $\Delta V_\Pi = a_\Pi\, e^{-\alpha_\Pi r}$ showed that the curvature of the experimental line $\vartheta(N)$ was not well described at small angles. Thus the ground potential was approximated by a simple Morse potential. The potential depth ε was assumed to be 0.3 eV, the equilibrium distance r_m to be 2.0 Å. The calculation showed that using this ground potential a good fit could be obtained at all energies. The results of the fitting procedure are:

$$V_{2\Pi_u} = V_{2\Pi_g} + 160.0\, e^{-3.0r} \quad \text{with} \quad (12)$$

$$V_{2\Pi_g} = 0.3\,(e^{9.0(1-\varrho)} - 2\, e^{4.5(1-\varrho)}) \quad \text{with} \quad \varrho = r/2.0\,.$$

These potentials are plotted in Figure 2. For the sake of comparison a potential of Lane and Everhart has also been plotted, which was deduced from high energy differential scattering data using an inversion procedure [13]. It represents an average $Ne^+ - Ne$ interaction potential for very small distances, which has been extrapolated in Fig. 2 to large distances. This potential was used as a ground potential by other investigators [14–17]. The dotted curve results from a theoretical formula by Bohr which describes the repulsive part of the potential between two atoms at small distances [13].

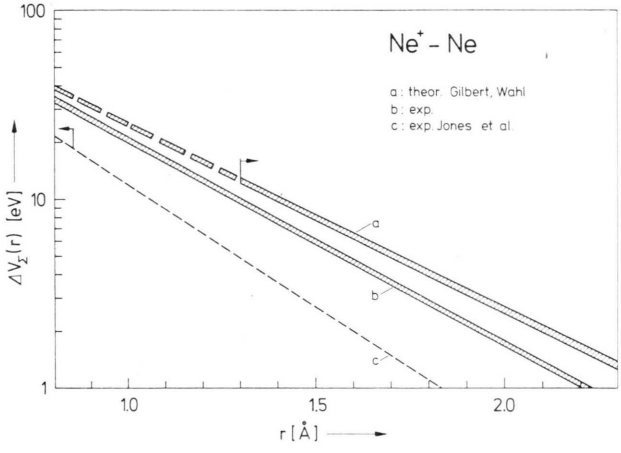

Fig. 6. Potential energy difference $\Delta V_\Sigma = V_{2\Sigma_g^+} - V_{2\Sigma_u^+}$ for the Ne_2^+-system. The arrows indicate the ranges of validity. a) Theoretical calculation by Gilbert and Wahl [3]. The results obtained by using various approximations lie within the shadowed area. b) Experimental result of this work. The width of the shadowed area corresponds to the experimental error. c) Experimental result from Jones et al. [15].

Figure 6 shows the difference potentials ΔV_Σ on a half-logarithmic scale. The shadowed region (curve a) contains all potentials which have been calculated by Gilbert and Wahl by different methods and for different distances [3]. The range of validity of their calculations lies right of the arrow pointing to larger distances. Curve b represents the experimental result of this work. The width of the shadowed region corresponds to the experimental error. The maximum difference between the theoretical and the experimental curves is about 40% in the range be-

tween 1 Å and 2 Å. Curve c is an extrapolation of the difference potential found by Jones et al. from measurements of the differential cross-section for resonant charge transfer at high energies [3, 16].

This potential is valid in the range from 0.63 Å up to 0.85 Å. The large discrepancy in curves b and c at small distances is most probably due to the use of the ground potential of Lane and Everhard (Fig. 2) which has been extrapolated to the range of internuclear distance which is covered by the experiments of Jones et al. Thus curve c can scarcely be compared with the curves a and b.

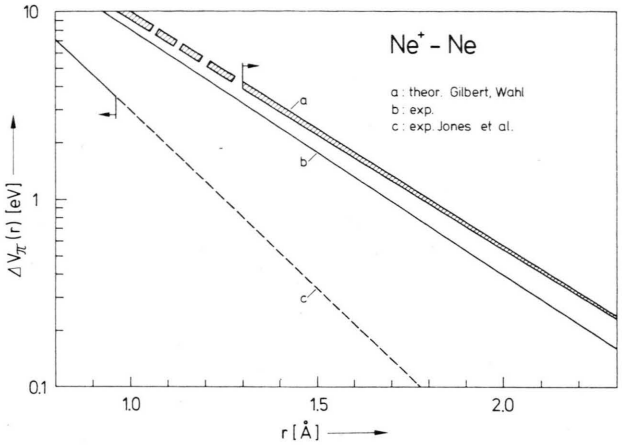

Fig. 7. Potential energy difference $\Delta V_{\Pi}=V_{^2\Pi_u}-V_{^2\Pi_g}$ for the Ne_2^+-system. The arrows indicate the ranges of validity. a) Theoretical calculation by Gilbert and Wahl [3]. The results obtained from various computational methods lie within the shadowed area. b) Experimental result of this work. c) Experimental result from Jones et al. [15].

Figure 7 shows the corresponding ΔV_{Π} difference potential in an analogous way as in Figure 6. The agreement between the theoretical curve a due to Gilbert and Wahl and the curve b which was determined in this investigation is better than for the ΔV_{Σ}-potential. The disagreement with curve c is much more marked than in Fig. 6 and is probably also due to the fact that Jones et al. used the potential of Lane and Everhart for the evaluation of the $\Pi_{g\text{-}u}$-oscillations.

On evaluating the observed rainbow structure, it was suggested that the equilibrium distance of the calculated $^2\Sigma_u^+$-potential curve is too small. If the evaluation procedure for the $\Sigma_{g\text{-}u}$- and the $\Pi_{g\text{-}u}$-oscillations is made with a larger value of r_m, larger values for the difference potentials are obtained according to relations given in Table II which would improve the agreement between theory and experiment.

b) $Ar^+ - Ar$

The differential cross-sections for the system $Ar^+ - Ar$ were measured in the energy range from $E_L = 7$ eV to 160 eV. At all energies $\Pi_{g\text{-}u}$-interferences could be observed, but no $\Sigma_{g\text{-}u}$-oscillations. Figure 8 shows two typical differential cross-sections

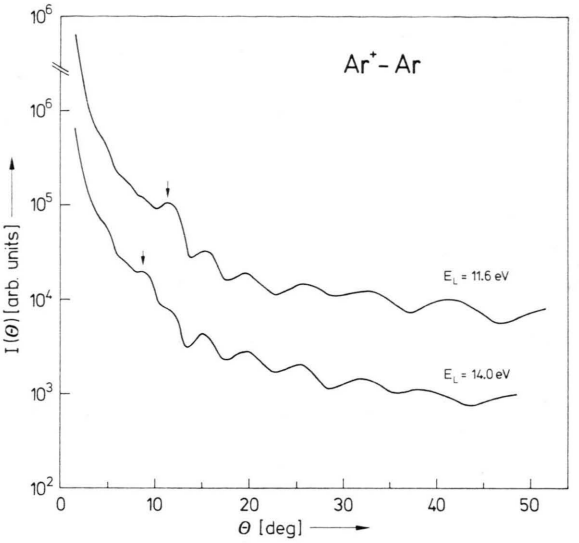

Fig. 8. Differential cross-sections for elastic $Ar^+ - Ar$-collisions at $E_L = 11.6$ eV and $E_L = 14.0$ eV. The arrows indicate the positions of the primary rainbow maxima.

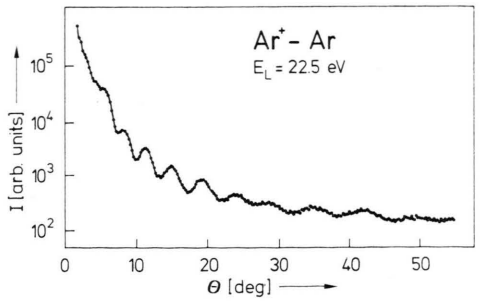

Fig. 9. Differential elastic scattering cross-section for $Ar^+ - Ar$ at $E_L = 22.5$ eV exhibiting $\Pi_g - \Pi_u$-oscillations.

at low energies with $\Pi_{g\text{-}u}$-interferences and a primary rainbow maximum at small angles. In Fig. 9 a differential cross-section for $E_L = 22.5$ eV is plotted. The oscillations are well pronounced up to $\Theta = 20°$. At larger angles the amplitudes are considerably quenched. This damping can be observed for E_L as low as 12 eV at large angles. At higher energies the

amplitudes of the oscillations become increasingly irregular as a function of the angle. Some minima are especially well pronounced. This suggests a superposition of oscillations with different frequencies. The irregularities at low energies are probably due to the spin-orbit coupling which can no longer be neglected. At higher energies inelastic processes caused by potential curve crossings (or pseudo-crossings) may contribute to the irregularity of the interference structure in the differential elastic scattering cross-section. For the evaluation of the $\Pi_{g,u}$-oscillations the $^2\Pi_g$-potential was constructed as for the system $Ne^+ - Ne$ using the condition that the two Π-potentials must lie between the Σ-potentials. The reduced potential and the equilibrium distance for the $^2\Sigma_u^+$-ground potential were taken from the calculation [3]. For the potential depth ε the value determined from rainbow scattering was used. The $^2\Sigma_g^+$-potential was obtained by adding the difference potential ΔV_Σ given by the theoretical calculation. The difference potential ΔV_Π was determined by variation of a and α in the same way as previously described. For $E_L \leqq 16$ eV, a good fit to the experimental data was obtained with the following potentials:

$$V_{^2\Pi_u} = V_{^2\Pi_g} + 210.0\, e^{-2.15r} \quad \text{with} \tag{13}$$

$$V_{^2\Pi_g} = 0.3\,(e^{9.86(1-\varrho)} - 2\, e^{4.93(1-\varrho)}) \quad \text{with} \quad \varrho = r/2.8\,.$$

The agreement between the curves $\vartheta(N)$ calculated with this potential and the experimental ones becomes less satisfying at higher energies for large angles. The experimental curves have a smaller slope than the calculated ones. According to Table II a fit can be obtained with a slightly decreased α, but then the agreement at small angles is not satisfying.

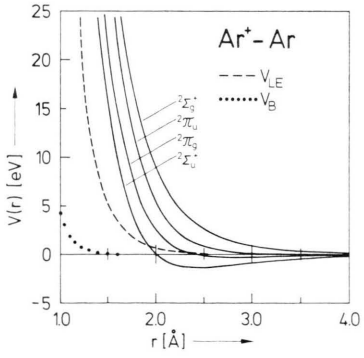

Fig. 10. Potential energy diagram of the four lowest states of Ar_2^+. Solid line curves: results of this work. Dashed line: results from Lane and Everhart [13] extrapolated to large internuclear distances. Dotted curve: repulsive Ar_2^+-potential calculated from the Bohr formula [13].

In Fig. 10 the potential curves of the system $Ar^+ - Ar$ are plotted as in Figure 2. The difference potential ΔV_Π is shown in Fig. 11 as a function of the distance. The agreement between the experimental and the theoretical result is much better than for the case $Ne^+ - Ne$. The somewhat arbitrary choice of the $^2\Pi_g$-ground potential does not influence severely the result for ΔV_Π. If the $^2\Pi_g$-potential is varied within reasonable limits, the fitting procedure leads to a difference potential which is very close to the result given by Equation (13). Good agreement between experimental and theoretical values has also been obtained for the potential depth of the $^2\Sigma_u^+$-ground state. Curve c has been obtained by Jones et al. [15] for the range from 0.9 – 1.7 Å by measurements at high energies using the potential of Lane and Everhart. As for the system $Ne^+ - Ne$ the difference between curves c and b is very large.

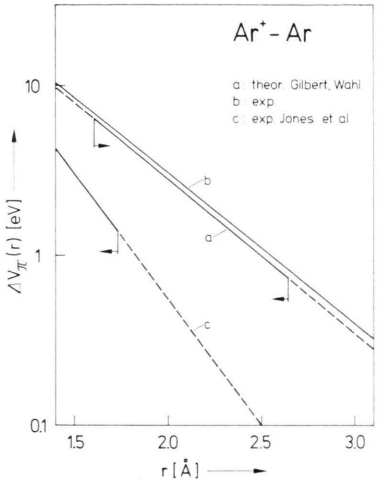

Fig. 11. Potential energy difference $\Delta V_\Pi = V_{^2\Pi_u} - V_{^2\Pi_g}$ for Ar_2^+. The arrows indicate the regions of validity. a) theoretical result from Gilbert and Wahl [3]; b) experimental result of this work; c) experimental result from Jones et alias [15].

c) $Kr^+ - Kr$

Figure 12 shows differential cross-sections for the system $Kr^+ - Kr$ at various energies. The arrows on the upper curves point to the primary rainbows which are caused by the attractive part of the ground state potential. As for the system $Ar^+ - Ar$ marked irregularities can be observed in the interference structure at energies $E_L \geqq 14$ eV.

The irregularities in the differential elastic scattering cross-section at low energies are probably due to spin orbit coupling which leads to fine structure

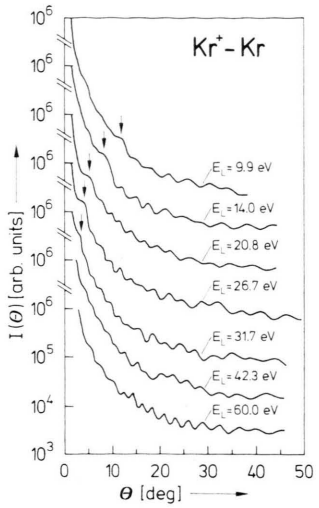

Fig. 12. Differential cross-sections for elastic $Kr^+ - Kr$ collisions at various energies (lab.-system). The arrows indicate the positions of the primary rainbow maxima.

splitting of the Π-states. The potential curve diagram is similar to that one shown in Fig. 3 for the system $Xe^+ - Xe$. Interference may occur between the states

$$(^2\Sigma_u^+)\,\tfrac{1}{2}\,u \quad \text{and} \quad (^2\Pi_g)\,\tfrac{1}{2}\,g\,,\ (^2\Pi_g)\,\tfrac{3}{2}\,g$$
$$\text{and} \quad (^2\Pi_u)\,\tfrac{3}{2}\,u\,,\ (^2\Pi_u)\,\tfrac{1}{2}\,u \quad \text{and} \quad (^2\Sigma_g^+)\,\tfrac{1}{2}\,g\,.$$

g-u-interference between molecular states originating from different asymptotic states ($r \to \infty$) are not possible since the scattering will then be incoherent. If only $Kr^+(^2P_{3/2})$-ions were present in the primary ion beam two groups of oscillations with approximately the same frequencies would be observed on account of interference between $(^2\Sigma_u^+)\,\frac{1}{2}\,u$ and $(^2\Pi_g)\,\frac{1}{2}\,g$ and between $(^2\Pi_g)\,\frac{3}{2}\,g$ and $(^2\Pi_u)\,\frac{3}{2}\,u$. If the ion beam contains $Kr^+(^2P_{1/2})$-ions as well oscillations due to interference between $(^2\Sigma_g^+)\,\frac{1}{2}\,g$ and $(^2\Pi_u)\,\frac{1}{2}\,u$ may be superimposed. The potential curve diagram (Fig. 3) suggests a small energy difference between $(^2\Sigma_g^+)\,\frac{1}{2}\,g$ and $(^2\Pi_u)\,\frac{1}{2}\,u$ and thus a large period of the corresponding g-u-oscillations. Hence the complexity of the experimental cross-sections may be explained by superposition of oscillations with different frequencies. At high energies inelastic processes may also disturb the differential elastic scattering cross-sections.

The evaluation of the experimental curves was performed under the assumption that the main contribution to the oscillatory structure is due to interference between $(^2\Pi_g)\,\frac{3}{2}\,g$ and $(^2\Pi_u)\,\frac{3}{2}\,u$. Using a reasonable guess for the $(^2\Pi_g)\,\frac{3}{2}\,g$-potential curve the difference $\Delta V_{3/2\,g-3/2\,u}$ was obtained from the fitting procedure:

$$V_{3/2\,u} = V_{3/2\,g} + 200.0\,e^{-2.07r} \quad \text{with} \tag{14}$$
$$V_{3/2\,g} = 0.3\,(e^{9.6(1-\varrho)} - 2\,e^{4.8(1-\varrho)}) \quad \text{with} \quad \varrho = r/3.0\,.$$

In the energy range from $E_L = 5$ eV to 10 eV there was satisfying agreement between the experimental results and the data calculated from the potentials of Equation (14). At higher energies the exponent α had to be varied from 2.07 to 2.02 at $E_L = 60$ eV. With a more elaborate analytical model potential a good fit could probably be obtained over a wider range of energies. Furthermore a more detailed analysis of the complex oscillatory structure should also yield information about the other potential curves.

d) $Xe^+ - Xe$

The differential cross-sections for $Xe^+ - Xe$ were measured in the energy range from $E_L = 6$ eV to 65 eV. In Fig. 13 several angular distributions are

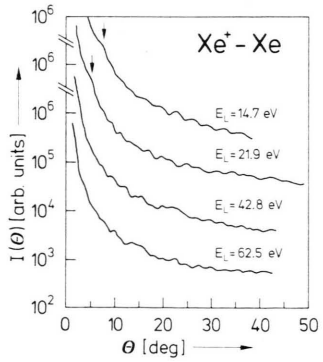

Fig. 13. Differential cross-sections for elastic scattering of Xe^+ on Xe at various energies. The arrows indicate the positions of the primary rainbow maxima.

shown. The arrows point to the primary rainbow maxima which could be observed in the energy range from $E_L = 6$ eV to 22 eV. g-u-oscillations could clearly be resolved only for $E_L \geqq 13$ eV. The differential cross-sections at higher energies show the same features as in the $Kr^+ - Kr$ system, but the irregularities are still more pronounced. They probably have the same causes as described for the sys-

tem $Kr^+ - Kr$. The evaluation was made in the same way as for the previous system. With the potentials

$$V_{3/2u} = V_{3/2g} + 200.0\, e^{-2.0r} \quad \text{with} \qquad (15)$$
$$V_{3/2g} = 0.3\,(e^{9.5(1-\varrho)} - 2\, e^{4.75(1-\varrho)}) \quad \text{with} \quad \varrho = r/3.2$$

a good fit could be obtained at $E_L = 50$ eV over the whole angular range. At lower energies the exponent α had to be increased, but still the fit was not satisfactory for all angles. The accuracy of the evaluation could certainly be improved by using a more flexible model potential or an inversion procedure [19] which allows a more direct determination of the interaction potential from the experimental results.

[1] H.-P. Weise, H.-U. Mittmann, A. Ding, and A. Henglein, Z. Naturforsch. **26 a,** 1122 [1971].
[2] H.-U. Mittmann, H.-P. Weise, A. Ding, and A. Henglein, Z. Naturforsch. **26 a,** 1112 [1971].
[3] T. L. Gilbert and A. C. Wahl, J. Chem. Phys. **55,** 5247 [1971].
[4] R. S. Mulliken, J. Chem. Phys. **52,** 5170 [1970].
[5] G. J. Lockwood, H. F. Helbig, and E. Everhart, Phys. Rev. **132,** 2078 [1963].
[6] D. C. Lorents and W. Aberth, Phys. Rev. **139,** A 1017 [1965].
[7] R. P. Marchi and F. T. Smith, Phys. Rev. **139,** A 1025 [1965].
[8] G. Herzberg, Molecular Spectra and Molecular Structure, Van Nostrand, New York 1950, Vol. I, Diatomic molecules.
[9] L. D. Landau and E. M. Lifshitz, Quantenmechanik, Akademie-Verlag, Berlin 1971.
[10] N. F. Mott and H. S. W. Massey, The Theory of Atomic Collisions, Oxford at the Clarendon Press 1965.
[11] D. Beck in "Proceedings of the International School of Physics Enrico Fermi Course XLIV. Molecular Beams and Reaction Kinetics", Academic Press, New York, London 1970, Ed. Ch. Schlier.
[12] M. Abramowitz and I. A. Stegun (Edit.) "Handbook of Mathematical Functions", Dover Publications, New York 1968.
[13] G. H. Lane and E. Everhart, Phys. Rev. **120,** 2064 [1960].
[14] P. R. Jones, P. Costigan, and G. Van Dyk, Phys. Rev. **129,** 211 [1963].
[15] P. R. Jones, N. W. Eddy, H. P. Gilman, A. K. Jhaveri, and G. Van Dyk, Phys. Rev. **147,** 76 [1966].
[16] P. R. Jones, T. L. Batra, and H. A. Ranga, Phys. Rev. Letters **17,** 281 [1966].
[17] M. Barat, J. Baudon, M. Abignoli, and J. C. Houver, J. Phys. B (Atom. Mol. Phys.) **3,** 230 [1970].
[18] B. K. Gupta and F. A. Matsen, J. Chem. Phys. **47,** 4860 [1967].
[19] M. Kennedy and F. J. Smith, Mol. Physics **16,** 131 [1969].